Characteristics of the flow around conventional and supercritical airfoils

Nakayama, A.

Characteristics of the flow around conventional and supercritical airfoils

By A. NAKAYAMA

Aerodynamics Research and Technology Department, Douglas Aircraft Company,
Long Beach, California 90846

Measurements of the mean and fluctuating velocities have been obtained with pressure and hot-wire probes in the attached boundary layers and wakes of two airfoil models at a low Mach number. The first model is a conventional airfoil at zero incidence and the second an advanced supercritical airfoil at an angle of attack of 4°. The mean-flow and Reynolds-stress data and related quantities are presented with emphasis on the trailing-edge region. The results indicate that the flow around the conventional airfoil is a minor perturbation of a symmetric flat-plate flow with small wake curvature and weak viscous–inviscid interaction. The flow around the supercritical airfoil is in considerable contrast with strong streamwise pressure gradients, non-negligible normal pressure gradients, and large surface and streamline curvatures of the trailing-edge flow. The near wake is strongly curved and intense mixing occurs between the retarded upper-surface boundary layer and strongly accelerated lower-surface boundary layer.

1. Introduction

The flow near the trailing edge of an airfoil can be complex even when the flow is attached, since the boundary layers that develop over the upper and lower surfaces lose the restrictions imposed by the surfaces as they start to merge and influence each other. As the surface restrictions disappear the flow directions depend increasingly on the entire flow field. The two boundary layers meet at an angle, merge and curve back smoothly to the freestream direction. If this process takes place over a short distance relative to the initial wake width, the pressure field is highly perturbed and interacts with the turbulent-stress field to influence the way the shear flow develops. These processes result in what is termed a strong viscous–inviscid interaction due to the interdependence of the viscous and inviscid flows.

Even when the flows do not curve, as in the case of a thin flat plate at zero incidence, the sudden loss of skin friction induces local pressure gradients due to the inevitably large streamwise stress gradients, see for example Melnik, Chow, and Mead (1977). The flows near the trailing edges of airfoils at angle of attack are further complicated by the streamwise pressure gradient and the variation of pressure across the boundary layer and near wake. These effects are particularly important near the trailing edges of supercritical airfoils with their emphasis on aft loading. Methods found to be successful in calculating near-wake flows work only for symmetric cases (Pope & Whitelaw 1976; Baker *et al.* 1982; Patel & Scheuerer 1982) in either zero or small pressure gradients and, as a result, with small streamline curvatures. To represent the pressure gradients and streamline curvature, methods based on the time-averaged

Navier–Stokes equations are becoming more common (Deiwert 1978; Viswanath *et al.* 1979; Wu & Gulcat 1981; Hah & Lakshiminarayana 1982; Adair, Thompson & Whitelaw 1983), but they have not yet been proven more successful. One of the problems is that, as pointed out by Bradshaw (1975), extra mean strain rates due to the abovementioned effects create large deviations in Reynolds-stress characteristics and major alterations to conventional turbulence models will be necessary to represent properly extra effects which make Navier–Stokes-like governing equations, instead of thin shear-layer equations, necessary.

Development of turbulence models that can reliably represent trailing-edge flows is hampered by the lack of detailed experimental data. Systematic experimental investigation of turbulent transport mechanisms that extend the simple flat-plate flows for which extensive data are now available (Pot 1979; Andreopoulos & Bradshaw 1980; Ramaprian, Patel & Sastry 1982) may eventually be required, but detailed samples of particular but typical flows also have great value in adding to the understanding of the flow characteristics which lead to identifying what may be satisfactorily predicted and what needs improvement.

Recent experimental investigations such as those made by Yu (1981), Hah & Lakshiminarayana (1982), Johnson & Spaid (1983), Viswanath & Brown (1983), and Adair, Thompson & Whitelaw (1983), give mean-flow and Reynolds-stress data in trailing edge regions of airfoil, blade or airfoil-like models. These data increased the understanding of airfoil flows but also suggest the inadequacy of available data.

This paper presents the results of detailed surveys of flows around two airfoil models with vastly different characteristics which emphasize the behaviour of the mean flow, turbulent stresses and transport quantities of attached flows in the trailing-edge region at a low subsonic speed. Some of the data from the same study were also given in an earlier paper (Nakayama 1983). The detailed data of mean-flow and Reynolds-stress fields will be treated here and quantities related to the transport of Reynolds stresses and turbulent kinetic energy will be reported later.

2. Experimental arrangements and techniques

2.1. *Wind tunnel*

The experiments were conducted in the $38 \times 54 \times 120$ in. low-speed wind tunnel at Douglas Aircraft Company, Long Beach facility. This is an Aerolab series 87 closed-circuit tunnel driven by a C532D Curtis variable-pitch propeller and is capable of delivering a flow of up to about 70 m/s. For the present measurements, the tunnel was operated with a honeycomb and six screens at a fixed speed of 30 m/s, which corresponds to the Reynolds number based on chord of 1.2×10^6. The freestream-turbulence level under this condition was approximately 0.02 %. The flow uniformity over the 2 m portion of the test section utilized for the measurements was very good and generally the variations of the total and the static pressures were less than 1 % of the dynamic pressure.

2.2. *Models*

The two airfoil models, each of 61 cm chord, are shown in figure 1. Model A is a 10 %-thick conventional airfoil and Model B a 14 %-thick advanced supercritical airfoil. The two airfoils are vastly different in shape but one common feature is that the included angles at the trailing edge of Models A and B are 10.18° and 10.05°, respectively. The surface curvatures will be discussed in §3, but here it is noted that the lower surface of Model B is very curved. For the measurements Model A was
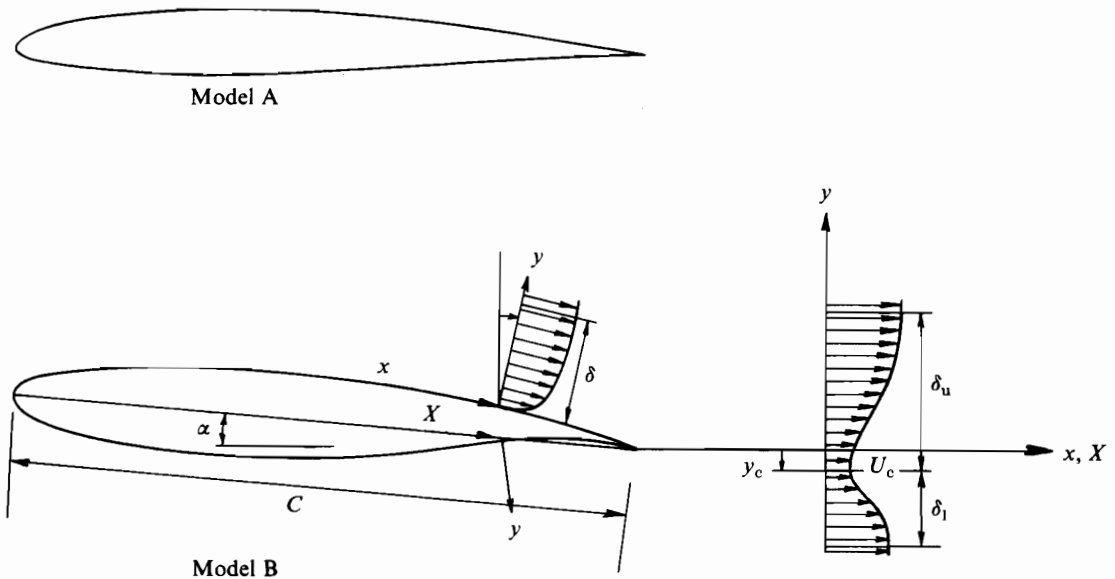
FIGURE 1. Airfoil profiles and definition of coordinates and notation.

located at the centreline of the tunnel at zero angle of attack while Model B was put at a geometric angle of attack of 4°. A number of pressure orifices were installed in chordwise and spanwise arrays on both models. The trailing-edge thicknesses are 0.6 mm on Model A and 0.18 mm on Model B, and backward-facing pressure orifices were placed to indicate the 'base pressure'. The trailing-edge thickness of Model A was comparable to the viscous-sublayer thickness while that of Model B was smaller.

On both models boundary layers were tripped at the same position: by a wire of diameter 1.3 mm at 16 % chord on the upper surface; and by a wire of diameter 0.5 mm at 5 % chord on the lower surface.

2.3. *Mean-flow measurements*

Surface pressures relative to p_{ref}, the pressure just downstream of the tunnel contraction, which can be regarded as the unperturbed freestream pressure, were measured by a strain-gauge pressure transducer of Stra Systems capacitance pressure transducer. Preston-tube measurements were obtained with three sizes (0.89, 1.60 and 3.23 mm o.d.) of L-shaped tubes tapered at the bottom so that they could be inserted in pressure orifices. The differences in the shear stress obtained by different sizes of tubes were within 2 %, except near the trailing edge. The spanwise distributions of the surface pressure, indicated by the spanwise arrays of pressure orifices, and the shear stress were found to be uniform within the measurement accuracy, indicating the closeness to two-dimensionality of the flow near the centreline.

Since it is an important part of the present measurements to find whether or not the static pressure within the boundary layer and the wake changes significantly, a static-pressure probe of standard NPL type was traversed in the trailing-edge region and in the wake, in addition to traversing total-head tubes. It is known that probes with static holes on the side are less reliable in a curved turbulent flow. In the present configurations, the maximum variation of the local flow direction was about 6° within a traverse and the maximum error could be maintained within about 3 % of the local

dynamic pressure by placing the probe in the average flow direction. The effect of turbulence on static-pressure probes is of the order of the square of the local turbulence intensity which could be about 15 % near the trailing edge; thus the errors due to turbulence could be about 3 % of the freestream dynamic pressure. It is not easy to correct for these errors and no corrections were made, but a check with the *y*-component momentum equation was made. The result of this check, discussed further in §3.1, indicates that the accuracy of the static pressure data is generally within 1 % of the dynamic pressure and about 3 % just downstream of the trailing edge of Model B where the turbulence intensities are rather large.

The total-pressure measurements were made by using a flattened tube of outside thickness 0.76 mm, both in the boundary layer and in the immediate vicinity of the trailing edge. In the rest of the wake a circular tube of outside diameter 1.6 mm was used. The yaw and turbulence effects on these probes are less serious than in the case of the static-pressure probe. All the pressure probes were calibrated against a standard probe, but no absolute calibrations were done.

All probes were traversed normal to the local surface in the boundary layers and vertically in the wakes, as shown in figure 1. In the case of the boundary layer, the traverse stations were chosen so as to cause the least interference with the static-pressure orifices. The most-downstream station was about 0.6 m upstream of the end of the test section.

2.4. *Turbulence measurements*

Turbulence measurements were made with two TSI 1050 hot-wire anemometers operated in the constant-temperature mode with 3.8 µm tungsten-wire sensors in a cross array. The probe was placed in the flow such that the plane of two sensors was parallel to the (x, y)-plane, where x is the distance along the body surface in the boundary layer or in the direction of the freestream in the wake, and y is the normal distance from the surface or vertically upward distance aft of the trailing edge (see figure 1). At a few selected stations the probe was also placed in the (x, z)-plane to check the two-dimensionality of the flow by measuring the shear stress $-\overline{uw}$ and also to obtain the magnitude of the spanwise fluctuation $\overline{w^2}$.

The anemometer outputs were analysed in two different ways. First, on-site analog analysis was performed to obtain the two mean-velocity components and the three Reynolds-stress components by using filters, sum and difference circuits, integrating voltmeters and r.m.s. meters. Signal linearizers were not used but the local sensitivity of the anemometers was evaluated using (1) below at every measurement point. Secondly, for the later off-site analysis, the output signals were band-pass filtered between 20 Hz and 20 kHz and recorded on a one-inch magnetic tape using a Sangamo Sabre III instrumentation tape recorder while the analog r.m.s. readings were made. The recorded signals were played back and digitized by a PDP11-34 mini-computer. The main purpose of the digital analysis was to compute higher-order moments and frequency spectra. The digital analysis included the inversion of the nonlinear calibration relations which were assumed to take the form

$$\frac{E^2}{T_{\mathrm{w}} - T_{\mathrm{f}}} = A U_{\mathrm{n}}^{0.45} + B, \qquad (1)$$

where E is the output voltage, T_{f} and T_{w} are the fluid and the wire temperatures, U_{n} is the velocity component normal to the effective direction of the wire, and A and B are calibration constants. This means that the cosine law for yaw response is assumed. To determine A, B and the effective direction of each wire, the probes were

calibrated before and after each traverse in the freestream. The effective direction of the wire was determined by rotating the wires in the (x, y)-plane at the calibration position using the method of Bradshaw (1971). A traverse was repeated whenever the calibrations showed any significant drift or deviation of the flow-direction response from the cosine law. The maximum drift accepted in the calibration constants A and B was 4 % and the values of A and B, interpolated in time between the initial and final calibrations, were used to reduce the data.

The accuracy of the hot-wire data was examined in several different ways. The mean-velocity results were compared with the Pitot-tube data. The agreement was excellent with differences of less than 1 % of U_{ref}, except in the immediate vicinity of the trailing edge of Model B. The variation of the normal component V of the mean velocity was consistent with the continuity equation and irrotationality condition outside the turbulent-flow region. The shear-stress results were checked with the x-component momentum equation and the wall values deduced from the Clauser-chart procedure.

Visual observations of smoke and tufts introduced in the trailing-edge region indicated that there was no boundary-layer separation. However, in a small region bounded by $y/C = 0$, 0.01 and $X/C = 1 \pm 0.03$ of Model B, the measured relative turbulent intensity exceeded 0.3, implying that the instantaneous velocity could be reversing in direction. The error in the turbulent-stress data in this small region is largest. The other area where the error could be significant is the region just downstream and below the trailing edge where the spatial resolution of the probe was not small enough. A conservative estimate of the accuracy of the turbulent-stress data in other regions is 5 % of the maximum in a profile.

3. Results and description of overall flow fields

The overall flow fields around the two models are represented by the surface pressure, edge-velocity distributions and momentum and displacement thicknesses in figures 2(a) and (b); and the static-pressure distribution and the mean-velocity vectors in the trailing-edge region in figures 3(a) and (b). The blockage effects due to the tunnel floor and ceiling were not negligible only in the sense that the surface pressures shown in figures 2(a) and (b) are somewhat lower and the wake trajectory in the downstream region is straighter than expected in free-air conditions. The surface-pressure distributions are typical of those over near-symmetric conventional airfoils and aft-loaded supercritical airfoils. The edge velocities U_e in the boundary layers and U_{eu} and U_{el} for the upper and lower edges of the wake shown in figures 2(a) and (b) were calculated from the measured total and static pressures. They correspond to the total velocities and are slightly larger than the x-direction components of the velocity. It should be noted that the difference between U_{eu} and U_{el} in the near wake of Model B is appreciable but not so in the same region of Model A. This, of course, implies that there is a pressure variation across the near wake of Model B. It does not, however, mean that there is no pressure variation across the near wake of Model A. The details of the pressure distribution are seen better in figures 3(a) and (b). The positions of the shear-layer edges were taken to be the points where the total-pressure defect from the external-flow value is 1 % of the maximum defect across the layer.

The displacement thickness δ^*, and the momentum thickness θ in the boundary layers were calculated from the usual definitions but, in the wake, they were calculated separately for upper and lower halves split at the minimum-velocity point
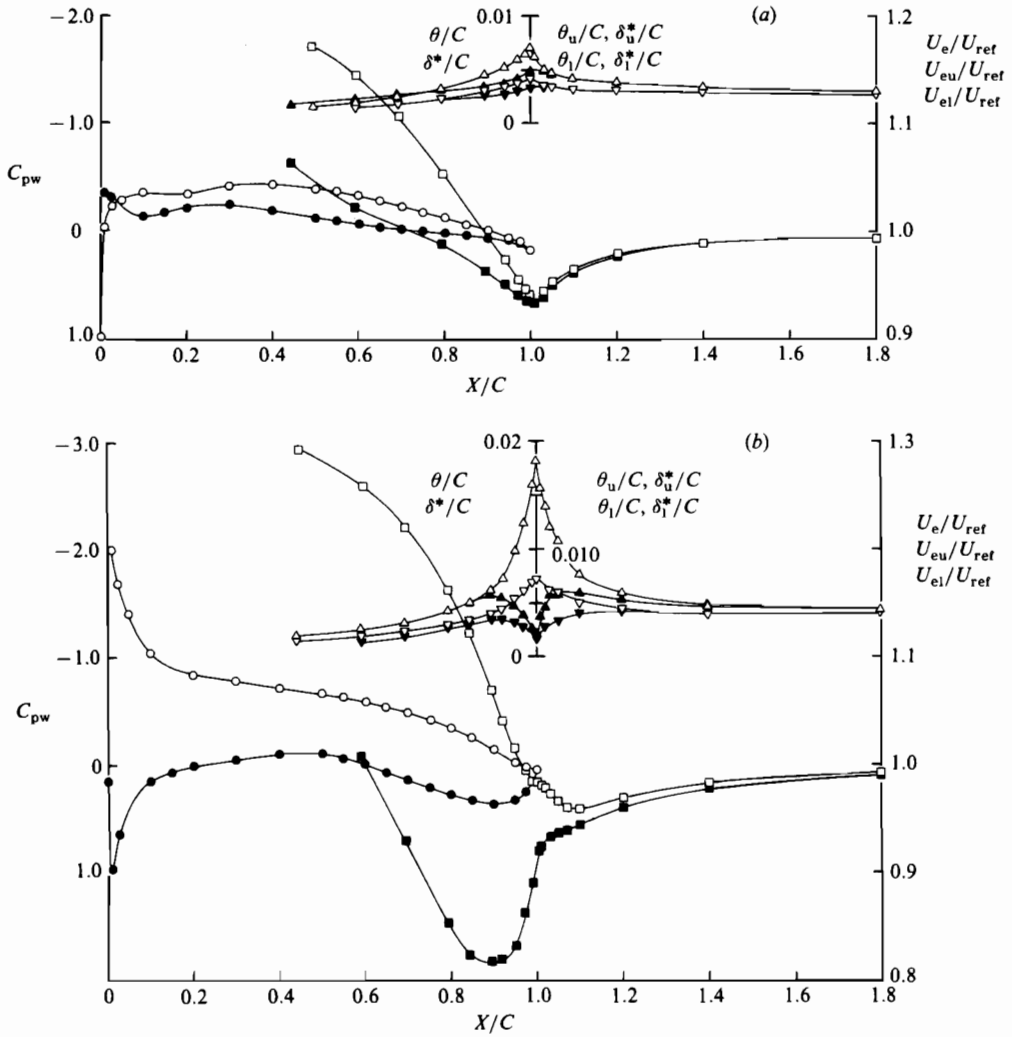
FIGURE 2. Surface pressure, edge velocity and momentum and displacement thicknesses, (a) Model A, $\alpha = 0°$, (b) Model B, $\alpha = 4°$: open symbols, upper side; closed symbols, lower side; $\bigcirc$, C_{pw}; $\square$, U_e/U_{ref}, U_{eu}/U_{ref} or U_{el}/U_{ref}; $\triangle$, δ^*/C, δ_u^*/C, or δ_l^*/C; ∇, θ/C, θ_u/C, or θ_l/C.

using the corresponding edge velocities. The results are plotted in figures 2(a) and (b). Subscripts u and l indicate quantities defined for the upper and lower halves of wake.

The isobar contours shown in figures 3(a) and (b) were constructed from the static-tube data. Since static-tube data obtained in curved turbulent flows are known to be inaccurate, the data were checked with the integrated y-component momentum equation:

$$C_p \equiv \frac{p - p_{ref}}{\frac{1}{2}\rho U_{ref}^2} = -2 \int \frac{1}{1+y/R_w} \left(\frac{U}{U_{ref}}\right)^2 \frac{\partial}{\partial x}\left(\frac{V}{U}\right) dy$$

$$+ 2\int \frac{1}{R_w + y} \frac{U^2 + V^2 - \overline{u^2} - \overline{v^2}}{U_{ref}^2} dy - 2\frac{\overline{v^2}}{U_{ref}^2} - 2\int \frac{1}{1+y/R_w}\frac{\partial}{\partial x}\frac{\overline{uv}}{U_{ref}^2} dy, \quad (2)$$

where R_w is the local radius of surface curvature (positive for convex upward for the upper surface and convex downward for the lower surface). The accompanying
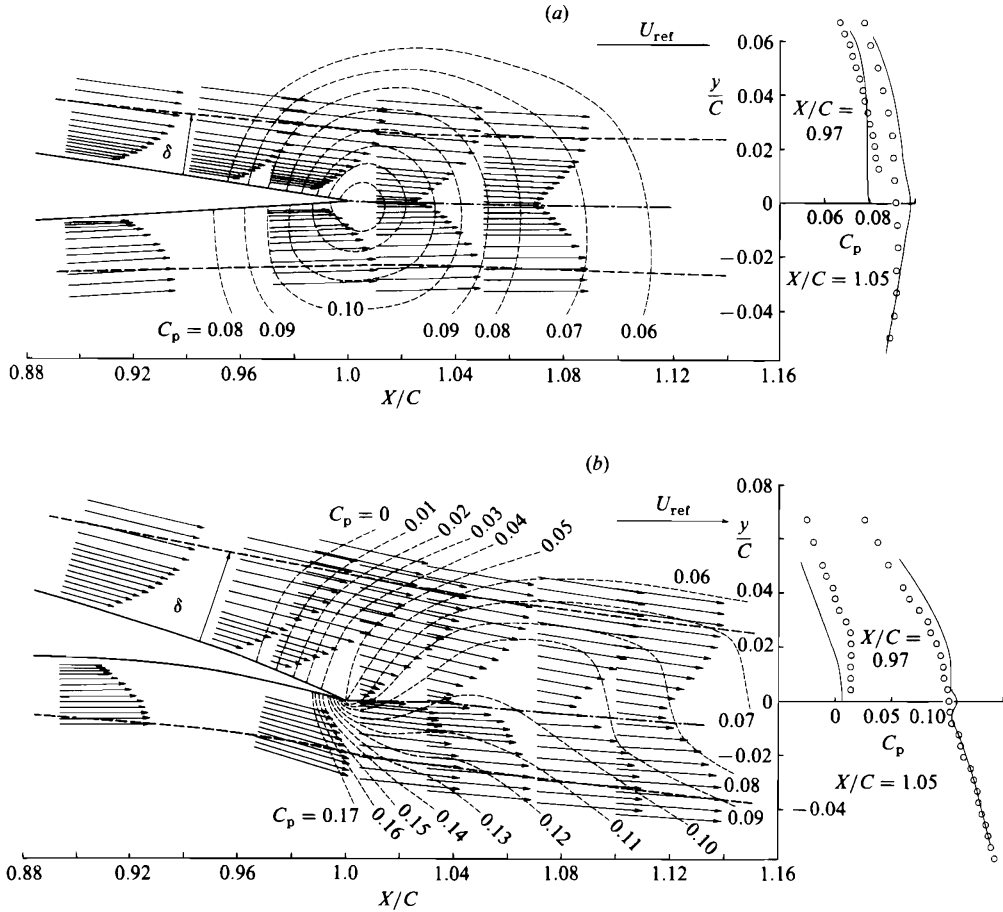
FIGURE 3. Static pressure distribution and mean-velocity vectors in the trailing-edge region, (a) Model A, $\alpha = 0°$, (b) Model B, $\alpha = 4°$: — · —, streamline starting at trailing edge; right hand part of figure shows pressure at $X/C = 0.97$ and 1.05; ○, static-probe data; ———, integration of y-component momentum equation.

cross-section plots of figures 3 (a) and (b) show the comparisons. The accuracy quoted earlier is confirmed.

The evaluation of various terms in the above equation revealed that the description of the pressure variation across the layer requires the full y-component momentum equation. The only terms that may be neglected are the turbulent stresses in the second term. The simplified form of this term $1/R_w \int (U^2/U_{ref}^2)\, dy$ is commonly used for curved flows with almost parallel streamlines. In the present flows this approximation is not very good, particularly near the trailing edge of Model B, where the actual pressure varies in the opposite way to that indicated by this term. In this region the first term is of larger magnitude and of opposite sign to this term. The third term, commonly used for straight flows with significant turbulent normal stress, is not representative of the way p varies across the layer either. The last term, which is due to the shear stress, was found to be important in the region just downstream of the trailing edge of Model B where a sharp peak in the shear-stress profile develops. Except for the importance of this shear-stress term in the near wake, the present

results agree with a similar analysis made by Wadcock (1980) for a separating boundary layer on an airfoil. If the coordinate system is aligned with the mean streamline, $V = 0$ everywhere and a somewhat simplified form of the equation may be used (Finnigan 1983).

Considerable qualitative differences are seen between the pressure fields of the two flows. The pressure is highest at the trailing edge of Model A and decreases in all directions. The boundary layers are decelerated but the wake is accelerated, in both cases by pressure gradients which are relatively mild. In the case of Model B, the highest pressure occurs at about 10 % chord upstream on the lower surface and the pressure within the flow decreases in the counter-clockwise direction around the trailing edge. The boundary layers experience opposite and strong pressure gradients so that the upper-surface boundary layer at the trailing edge is about 2.5 times thicker than that on the lower surface. The isobar contours indicate that the streamwise pressure gradients are larger near the surface than away from it. The pressure difference between the upper and lower edges of the wake is sufficient to cause nearly 6 % difference in the edge velocities. The upper half of the initial part of the wake up to about $X/C = 1.07$ is still decelerated while the lower half is accelerated.

The mean-velocity vectors superimposed on figure 3 show the general flow pattern in the trailing-edge region. The dividing streamline that starts at the trailing edge is also indicated in the same figures. The locus of the point of minimum velocity $y = y_c$ (referred to as the wake centreline hereafter) is not shown but it can be seen from the velocity profiles that it moves towards the thicker side relative to the positions of the trailing-edge streamline. The velocity vectors off the airfoil surface near the trailing edge gradually approach the freestream velocity. The feature of the streamlines near the trailing edge is that the way they curve is determined not only by the surface curvature but also by the trailing-edge angle and the orientation of the trailing edge with respect to the freestream direction. In the case of the conventional-airfoil Model A, the trailing-edge angle dictates the turning of the flow. The flow coming from the upper-surface boundary layer is bent at about 6° and that coming from the lower-surface boundary layer is deflected about 4°. The sum of about 10° is the enclosed angle of the trailing edge. The trailing-edge angle of Model B is also about 10° but the bisector is inclined about 15° from the freestream direction and the mean-velocity vectors in general curve upwards. The surface curvatures near the trailing edge are just opposite so that the streamline curvatures change considerably across the shear layer.

In order to show the features of the flow angularity and curvature more quanti-tatively, the streamwise variation of the streamline and surface curvatures are plotted in figures 4(a) and (b). The curvatures K_s of the streamlines are given at $y = 0, 0.2\delta$ and δ for the boundary layer, and $y = y_c$ (wake centre), $y_c + 0.2\delta_u$, $y_c - 0.2\delta_l$, and $y_c + \delta_u, y_c - \delta_l$ for the wake. K_s was calculated using the smoothed data and the formula

$$K_s = \frac{1}{R_s} = \left(\frac{U}{Q}\right)^3 \left[\frac{1}{1+y/R_w}\frac{\partial}{\partial X}\left(\frac{V}{U}\right) + \frac{V}{U}\frac{\partial}{\partial y}\left(\frac{V}{U}\right)\right] + \frac{U}{Q}\frac{1}{R_w+y}, \qquad (3)$$

where Q is the total mean velocity. The bracketed term represents the deviation from the curves parallel to the surface whose curvature is $1/R_w$. The boundary-layer thickness is also shown in the same figures so that the radius of curvature may be compared with the local boundary-layer thickness. The surface curvatures of the supercritical airfoil model are seen to be much larger than those of the conventional airfoil. In both cases, in the boundary layers upstream of about $X/C = 0.80$, the surface curvature and the curvatures of the streamlines at $y/\delta = 0.2$ and 1.0
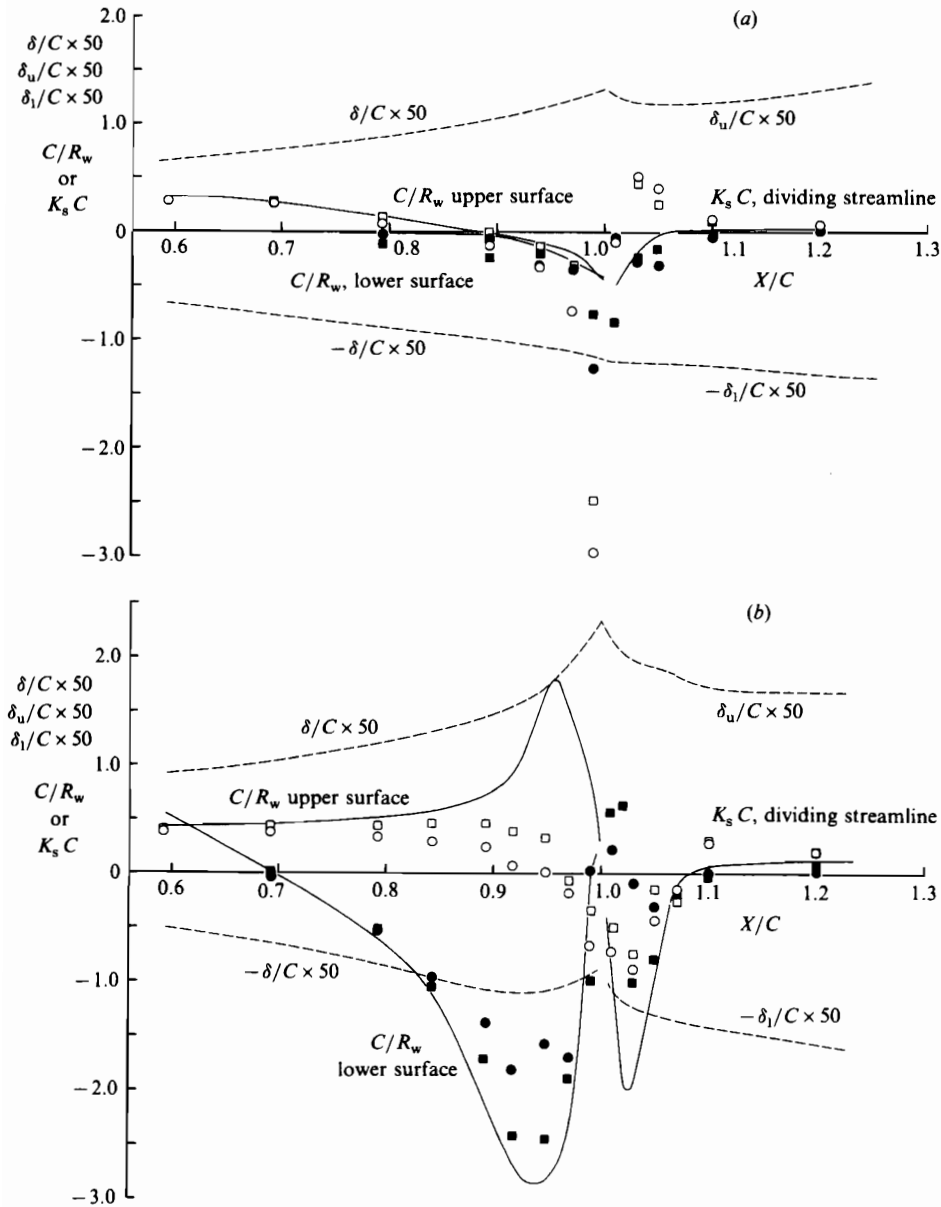
FIGURE 4. Streamline curvatures, (a) Model A, $\alpha = 0°$, (b) Model B, $\alpha = 4°$: open symbols, upper-surface boundary layers or upper half of wake; closed symbols, lower-surface boundary layers or lower half of wake; ———, surface curvature or curvature of streamline starting at trailing edge; ---, boundary layer or wake thickness; $\square$ streamline curvature at $y/\delta = 0.2$, $(y-y_c)/\delta_u = 0.2$ or $(y_c-y)/\delta_1 = 0.2$; $\bigcirc$ at $y/\delta = 1$, $(y-y_c)/\delta_u = 1$ or $(y_c-y)/\delta_1 = 1$.

all coincide. In the region near the trailing edge they are different. In the case of Model A, in a small region near $X/C = 1.0$, the streamlines have curvatures that are considerably larger than the surface curvatures. In the case of Model B, the streamline curvatures are smaller than the surface curvatures over the aft 20 % chord. In the upper-surface boundary layer, very close to the trailing edge, the streamline curvatures at $y/\delta = 0.2$ and 1.0 are opposite to that of the surface. In most curved

flows in which curvature effects have been studied, K_s can be well approximated by the last term in (3), which indicates a small linear variation across the flow. In the present flows near the trailing edges of airfoils, the changes in the last term are not significant and the difference in the values of R_s and R_w is mainly due to the deviation from parallel flow that is represented by the first term in (3). This variation of K_s across the shear layer takes place mostly near the surface $y/\delta \leqslant 0.20$ so that the flow is nearly parallel throughout most of the outer layer but at an angle to the local surface.

4. Mean-velocity data

Qualitative features of the mean velocities can be clearly seen in the vector plots already presented in figures 3(a) and (b)). Figure 3(a) shows that the mean-velocity field near the trailing edge of Model A is similar to that of a flat-plate flow and, in the wake, very close to the symmetric airfoil flow measured by Yu (1981). The mean-velocity profile on the upper side of the trailing edge of model B is, however, very close to separation. The lower-surface boundary layer is accelerated sharply, resulting in a highly asymmetric near wake. The region just downstream of the trailing edge looks more like a mixing layer sandwiched by two boundary layers.

The mixing-layer-like behaviour of strongly asymmetric near-wake flow was also observed by Cleary *et al.* (1980) and Viswanath & Brown (1983) who also visualized a large-scale vortex structure similar to that in plane mixing layers. It is likely that such a large structure exists just below the centreline of the near wake of Model B, since the mean-velocity gradient there is as large as those measured by Viswanath & Brown (1983) and the Reynolds-stress data presented in the next section do indicate a similarity to a mixing layer. It is noted that the position of the minimum velocity initially moves towards the thicker side as has been confirmed by other workers who made measurements in asymmetric airfoil wakes.

The mean-velocity profiles in the boundary layers are also plotted in law-of-the-wall coordinates in figure 5. The log law is seen to be satisfied in the two boundary layers of Model A up to the trailing edge, while the boundary layers of Model B are influenced by strong pressure gradients and surface curvatures so that the velocity profiles deviate considerably from the log law. At the trailing edge both upper- and lower-surface boundary layers have almost lost the logarithmic form. In the near wake of flat plates measured by Chevray & Kovasznay (1969), and Andreopoulos & Bradshaw (1980), the log law continued into the initial part of the wake and near-wake-velocity profiles of the present Model A were examined to determine if this was true. It was found that the continuation of the inner layers of upstream boundary layers conformed with the universal log law but only if the origin for the distance y was taken on the smooth extension y_0 of the respective surface and the velocity scale u_τ was replaced by an effective scale $u_{\tau\,\mathrm{eff}}$. This effective velocity scale $u_{\tau\,\mathrm{eff}}$ was found by a trial-and-error method. The results are also shown in figure 5. The profiles at $X/C = 1.01$ are in terms of this $u_{\tau\,\mathrm{eff}}$ and $y - y_0$. They show a log law region. Little log-law region is seen at $X/C = 1.05$. Outer-layer similarity of boundary-layer-velocity profiles is discussed in §7.

5. Skin-friction data

The skin-friction coefficients were obtained from the Clauser chart and from a Preston tube and the results are shown on figure 6. Both methods rely on the inner-law similarity and have difficulties when the similarity is not confidently satisfied. The
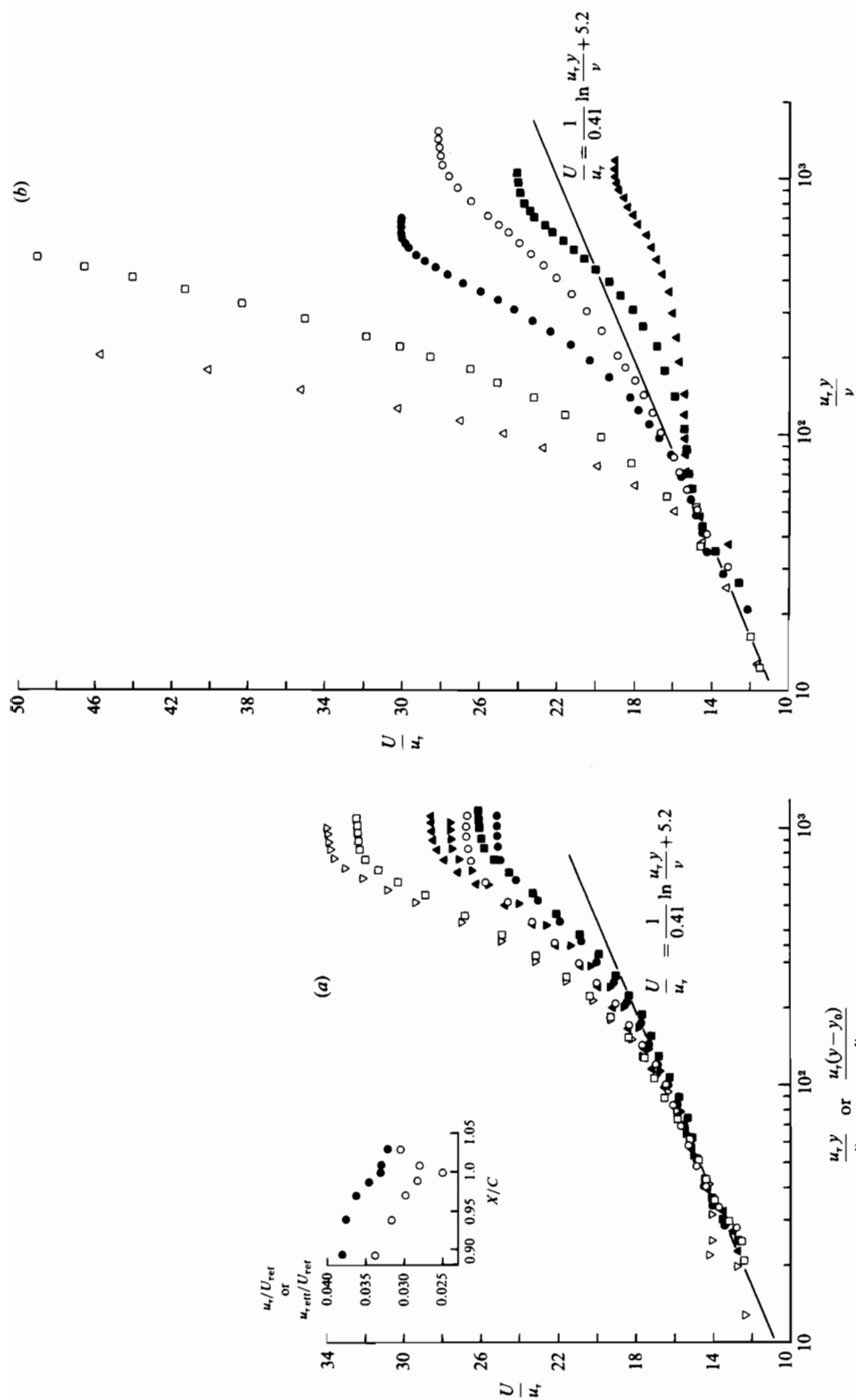
FIGURE 5. Logarithmic plot of mean velocity profiles, (*a*) Model A, $\alpha = 0°$, (*b*) Model B, $\alpha = 4°$: open symbols, upper-surface boundary layers or upper half of near wake; closed symbols, lower-surface boundary layers or lower half of near wake; $\bigcirc$, $X/C = 0.793$; $\square$, 0.97; $\triangle$, 1.0; $\triangledown$, 1.01.
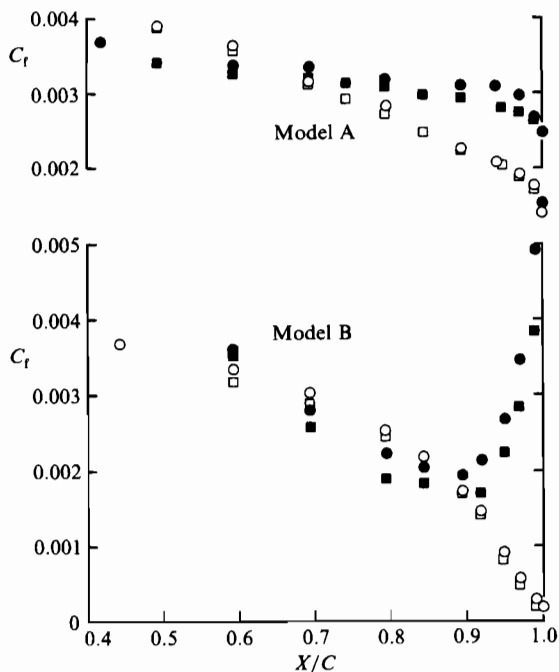
FIGURE 6. Skin-friction coefficient: open symbols, upper-surface boundary layers; closed symbols, lower-surface boundary layers; ○, log fit; □, Preston tube.

log law used to fit the inner-layer-velocity profiles is

$$\frac{U}{u_\tau} = \frac{1}{0.41}\ln\frac{u_\tau y}{\nu} + 5.2. \tag{4}$$

The Preston-tube data were analysed using Patel's (1965) calibration, and the C_f values obtained by these two methods should be consistent (Brederode & Bradshaw 1978). The value of the parameter used by Patel to indicate the severity of the limiting pressure gradient for a Preston tube to be valid, was found to exceed the limits for 6 % accuracy in the region $X/C \geqslant 0.9$ on both surfaces of Model B. A difficulty was also encountered in determining C_f by the log fit but the visual fitting was aided by the observation that the deviation from the log law is progressive from the larger value of $u_\tau y/\nu$.

6. Reynolds-stress data

The Reynolds normal stresses (divided by density) $\overline{u^2}$ and $\overline{v^2}$ are plotted in figures 7 (a) and (b) and the shear stresses $-\overline{uv}$ are shown in figures 8 (a) and (b). They are the results of the analog averaging of the unlinearized fluctuating signals from the hot-wire anemometers. These quantities were also calculated by digital methods which include the inversion of the nonlinear calibration relations, (1). The differences between the analog and digital results were generally within 5 % except in the high-intensity region, where in the near wake the digital results were about 10 % higher than the analog results. In the plots of the shear stress, the semicircles at $y = 0$ are $(u_\tau/U_{\text{ref}})^2$, where u_τ is determined by the log fit of the mean-velocity profiles. The extension of $-\overline{uv}$ onto the surface results in values which are in good agreement with
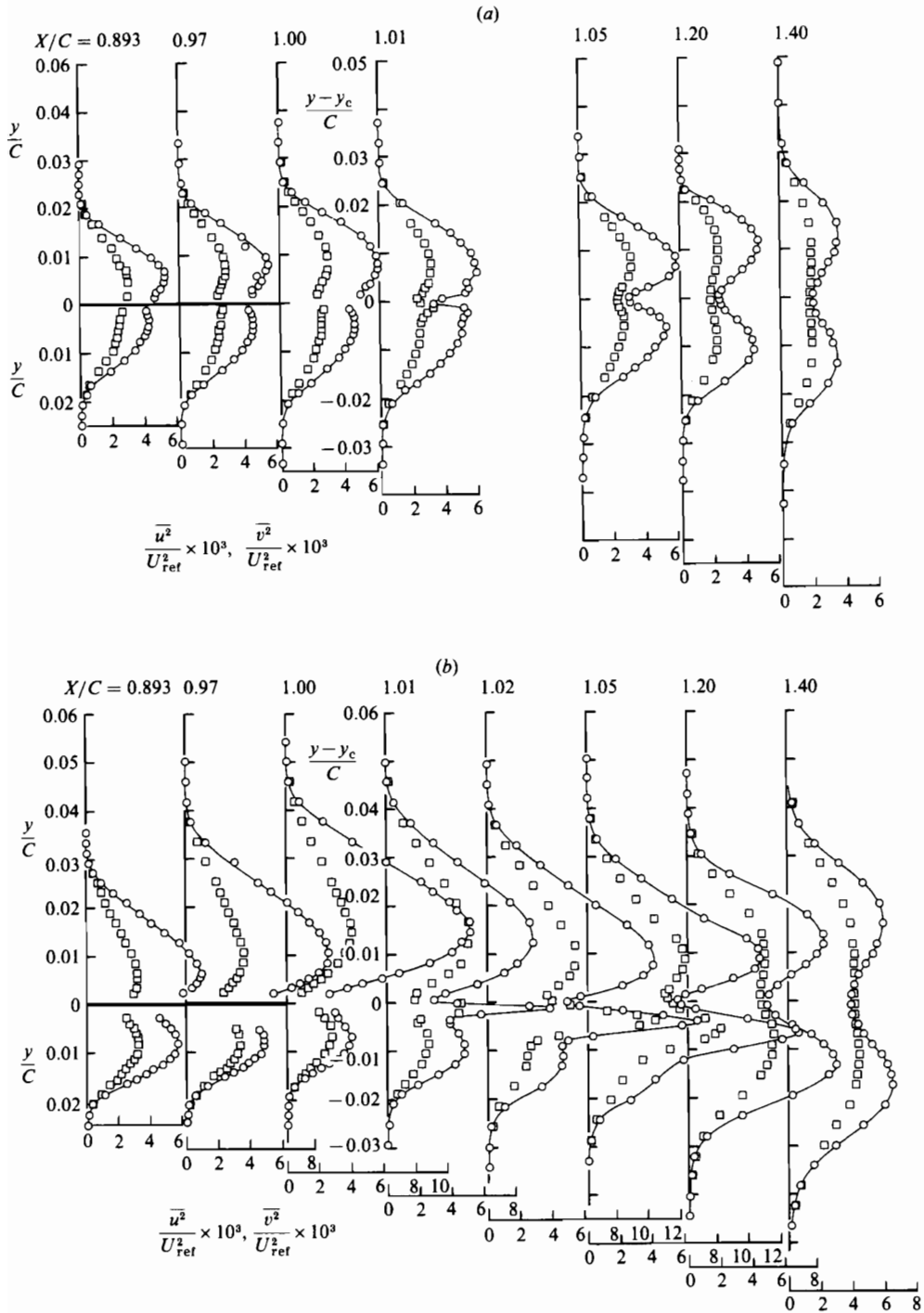
FIGURE 7. Reynolds-normal-stress distributions, (a) Model A, $\alpha = 0°$, (b) Model B, $\alpha = 4°$: ○, $\overline{u^2}/U_{\text{ref}}^2$; □, $\overline{v^2}/U_{\text{ref}}^2$.
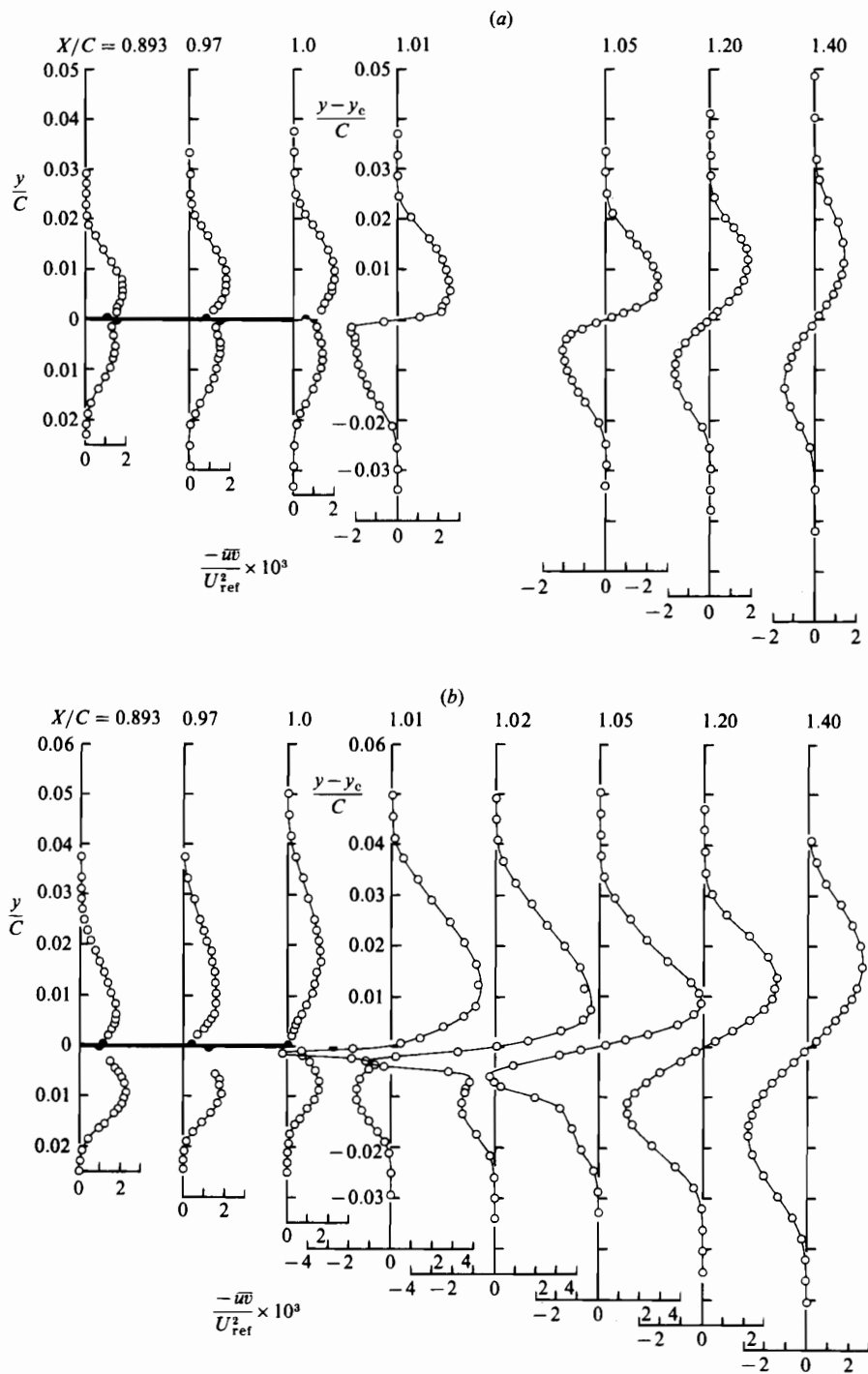
FIGURE 8. Reynolds-shear-stress distributions, (a) Model A, $\alpha = 0°$,
(b) Model B, $\alpha = 4°$: semicircles at $y = 0$ are $(u_\tau/U_{\mathrm{ref}})^2$.

Lower-surface boundary layer
or lower half of wake
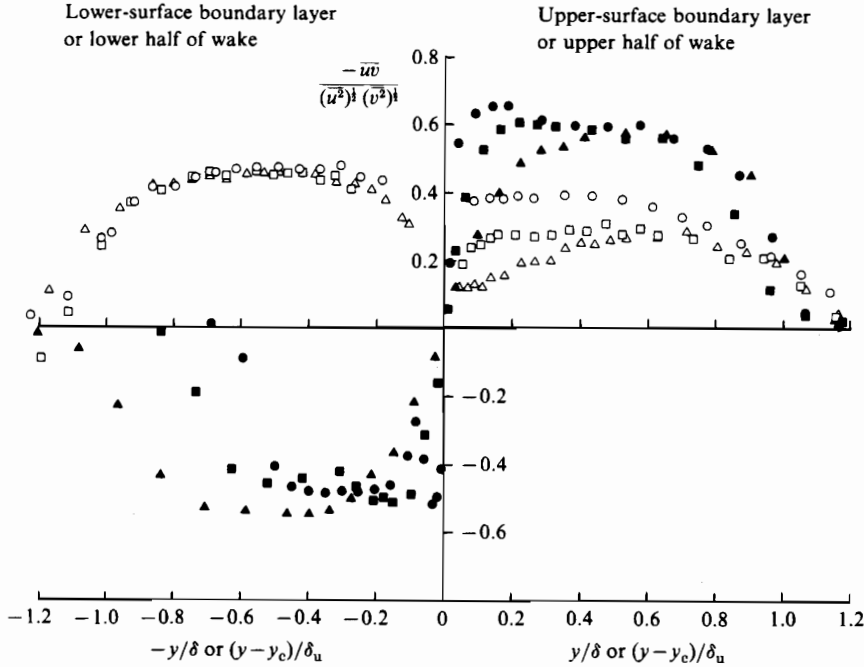
Upper-surface boundary layer
or upper half of wake

FIGURE 9. Shear correlation coefficient in the flows of Model B: $\bigcirc$, $X/C = 0.793$; $\square$, 0.97; $\triangle$, 1.0; $\bullet$, 1.01; $\blacksquare$, 1.05; $\blacktriangle$, 1.20.

u_τ^2 values, except in the lower-surface boundary layer of Model B near the trailing edge. The very large values of u_τ^2, compared with the small values of extrapolated $-\overline{uv}$ there, are due to the large favourable pressure gradient. The shear correlation coefficient, $-\overline{uv}/[(\overline{u^2})^{\frac{1}{2}}(\overline{v^2})^{\frac{1}{2}}]$ in the boundary layers and the wake of Model B is plotted in figure 9 to show the level of correlation.

The distributions of $\overline{u^2}$, $\overline{v^2}$ and $-\overline{uv}$ in the boundary layers of Model A show the well-accepted trends of those in weak adverse pressure gradients, i.e. increasing turbulent stresses with maximum stress points away from the walls. The development of these Reynolds stresses on Model B show some anomalous behaviour. On the upper surface over the region $0.5 \leqslant X/C \leqslant 1.0$ (the results are shown only for $X/C \geqslant 0.893$) the maximum values of longitudinal mean-square intensities $\overline{u^2}$ increase by about 70%, those of $-\overline{uv}$ reduce to about one half and those of $\overline{v^2}$ do not show much change. Noting that these stresses are plotted with U_{ref} as the normalizing velocity, $\overline{u^2}/U_\mathrm{e}^2$ increases by a factor of 2.5. Figure 9 shows that the level of the shear correlation coefficient also decreases. At $X/C = 1.0$ it is less than 0.3 and as small as the values obtained in the separated boundary layer of Simpson, Chew & Shivaprasad (1981a).

In the plots of the profiles in the wake, the vertical distances are relative to the positions of minimum velocity y_c. It appears that this choice of coordinates makes it easier to see the changes with respect to the mean velocity but it must be noted that the streamlines from the trailing edge take different trajectories: the locus of the minimum velocity initially moves up while the streamlines do not. The apparent jump or discontinuity between the last boundary-layer station and the first wake station is due mainly to the artificial rotation of the coordinate system rather than the shift in positions. The surface coordinate for the upper-surface boundary layer of Model B is rotated about 24° from that of the wake, which is aligned along the

direction of the free stream. As a result of this coordinate rotation, the maximum shear stress in the first station of the wake is about three times larger than that in the upper-surface coordinates of Model B. It is interesting to note that these jumps reverse much of the continuous changes that took place over the upstream boundary layer. It suggests that some part of the 'anomalous behaviour' described above is due to the inappropriate choice of the body-based coordinate system which exaggerates the departure from the thin boundary-layer characteristics.

In the region just downstream of the trailing edges, rapid changes are seen near the centreline and changes are very gradual outside. In both cases, the rapid changes are initiated right at the trailing edge and propagate outwards, showing the interacting region and uninfluenced outer wake more clearly than the development of mean-velocity profiles. The differences between the wakes of two models seen from the mean-velocity profiles are also evident. In the case of Model A, the interaction of the merging boundary layers is very weak. It is more symmetric and diffuses out quickly without changing the stress distribution greatly. It was noted by Ramaprian et al. (1982) that, in their data and in the data of Pot (1979), there are marked overshoots in the shear stress and $\overline{v^2}$ distributions very close to the trailing edges of flat plates. Ramaprian et al. associated these with the flow separation and vortex shedding at the finite-thickness trailing edge (about 1 mm). Similar peaks were seen in the airfoil wake data of Yu (1981). In the present data these overshoots are not seen. In the data of Model A plotted in figures 7(b) and 8(b), small peaks in $\overline{u^2}$ and $\overline{uv}$ are seen just outside the interacting inner wake at $X/C = 1.01$. In the case of Model B, very intense mixing between the two merging boundary layers creates sharp peaks in the stress distributions. These peaks are clearly different from the overshoots mentioned by Ramaprian et al. These peaks grow for some distance, up to about $X/C = 1.05$, which coincides with the point where the streamwise pressure gradient becomes favourable throughout the wake cross-section. At about the same position, the width of the upper half of the wake ceases to decrease and starts widening. Also the positions of maximum stress start to shift outwards. The interacting part of the wake for this case is one half of the more symmetric cases of flat-plate wakes or the wake of Model A, with only single peaks in the stress distributions which grow and migrate to the lower half of the wake, leaving the upper half free from direct influence.

It is useful to note that, in both cases, the zero shear stress occurs at the position where the mean-velocity gradient is zero. This is very clear at all stations except perhaps at the first measuring station in the wake of Model B and means that the production of turbulent kinetic energy is everywhere positive even without including the production due to the normal stresses. It also means that at no point is the eddy viscosity negative or the mixing length imaginary. The streamwise turbulent intensity takes a minimum at the same positions. The transverse intensity, however, assumes a local minimum slightly off y_c and $\overline{v^2}$ appears to have a local minimum on the side of lower turbulent intensity, i.e. on the lower side for Model A and on the upper side for Model B. At downstream stations, the dips in the $\overline{v^2}$ profiles disappear and both normal-stress profiles become very close to the flat-plate wake results of Chevray & Kovasznay (1969) and Andreopoulos & Bradshaw (1980).

7. Characteristics of the shear flow near the trailing edge of a supercritical airfoil

From the results presented so far, it can be said that the boundary layers near the trailing edge of an aft-chambered airfoil behave differently from those on flat surfaces or on curved surfaces with small pressure gradients. Understanding of this type of
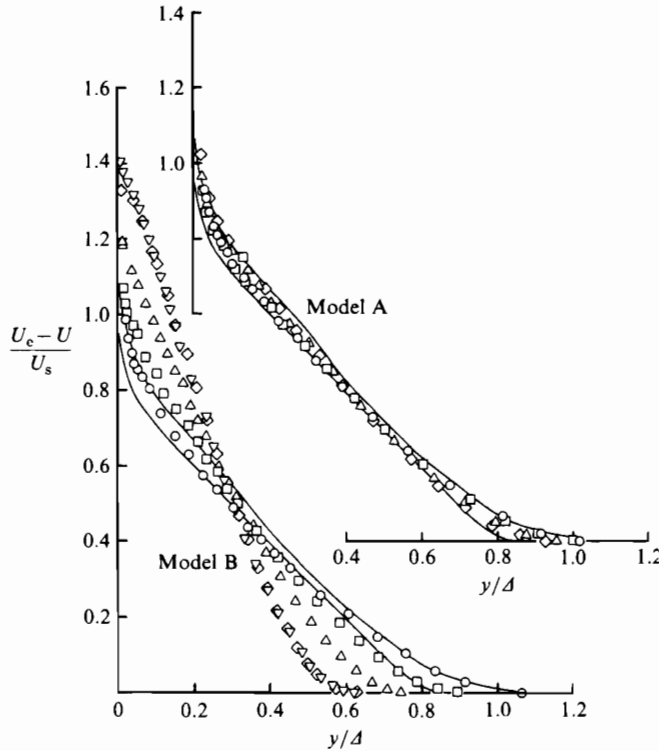
FIGURE 10. Mean-velocity profiles in the upper-surface boundary layer compared with Perry–Schofield (1973) profile: $\bigcirc$, $X/C = 0.793$; $\square$, 0.893; $\triangle$, 0.949; $\triangledown$, 0.97; $\diamondsuit$, 1.0; ——, limits of scatter in data used by Perry & Schofield.

shear flow is important since aft-chambered supercritical airfoils are an effective lift device, particularly at transonic speeds, and prediction methods are not satisfactory (Spaid & Hakkinen 1977; Johnson & Spaid 1983). The special features are related to the large and rapidly changing pressure gradients and streamline curvatures. There are several points that need to be examined and discussed with regard to the boundary layers on Model B, the supercritical airfoil.

The magnitude of the pressure gradients is indicated by parameters such as that of Clauser ($\beta = (\delta^*/\tau_{\rm w})\,\mathrm{d}p_{\rm w}/\mathrm{d}x$, where $\tau_{\rm w}$ and $p_{\rm w}$ are respectively the shear stress and pressure on the surface). β is greater than 20 over the aft 10 % of the chord on the upper surface and is as large as 80 very close to the trailing edge. On the lower surface it is smaller than -4.0 in the region $X/C \geqslant 0.94$. The deviation of the mean velocity from the usual logarithmic law is, therefore, severe. The pressure gradient is also responsible for the large gradients, with respect to y, of the Reynolds stresses near the surface. In the upper-surface boundary layer, the maximum shear stress $(-\overline{uv})_{\rm max}$ is well above 1.5 times the wall value. This suggests that the mean-velocity profiles in that region may be described by the universal velocity profile proposed by Perry & Schofield (1973) for boundary layers in moderate-to-strong adverse pressure gradients in which $(-\overline{uv})_{\rm max} \geqslant 1.5u_\tau^2$. The velocity scale $U_{\rm s}$ and the lengthscale $\varDelta$ for their outer layer and the overlap region between the inner and outer layers are given by

$$U_{\rm s} = 8\left(\frac{\varDelta}{L}\right)^{\frac{1}{2}} U_{\rm M}, \tag{5}$$

$$\varDelta = 2.86\delta^* \frac{U_e}{U_s},\tag{6}$$

where $U_M \equiv (-\overline{uv})^{\frac{1}{2}}_{max}$ and L is the distance from the wall to the maximum-shear location. The velocity profiles in terms of these similarity parameters as determined from the measured shear-stress profiles are shown in figure 10 and compared with the Perry–Schofield profile. The upper-surface boundary-layer data of the conventional airfoil Model A are also shown in the same figure since the condition $(-\overline{uv})_{max} \geqslant 1.5u_\tau^2$ is satisfied in this case as well. This figure shows that the velocity profiles on Model A agree very well with the Perry–Schofield profile while those on Model B deviate progressively as the trailing edge is approached.

Simpson, Strickland & Barr (1977) noted that the mean-velocity data taken in their boundary layer approaching separation agreed well with the Perry–Schofield profile if the 'pseudo shear stress' defined by

$$-\overline{uv} + \int_y^\infty \frac{\partial}{\partial x}(\overline{u^2} - \overline{v^2})\,\mathrm{d}y$$

was used to determine U_M and L instead of the shear stress itself. The reasoning behind this modification is that it accounts for the normal stresses which were found to be important in the flow of Simpson et al. (1977) but were ignored in Perry and Schofield's analysis of deducing the shear stress from the mean-velocity data that were not accompanied by turbulent-stress data. The normal stresses were found to be important in the present flows as well. The use of the pseudo shear stress of Simpson et al., however, assumes that the static pressure is given by

$$\frac{p}{\rho} = -\overline{v^2} + \frac{p_e}{\rho},$$

where p_e is the pressure at the edge of the boundary layer. In spite of the objection that this was not verified in the present flow, the approach using the pseudo shear stress was tried in order to correlate the mean-velocity data. The results for $X/C = 0.949, 0.97, 0.99$ and 1.0 are shown in figure 11. The figure indicates that the profiles in terms of the modified parameters come very close to the universal profile. It is noted, however, that the shape of the profiles at $X/C = 0.99$ and 1.0 are a little different from the Perry–Schofield profile in the region $y/\varDelta \leqslant 0.20$. This region corresponds to the half-power-law region which was shown by Perry and Schofield to be just outside the usual logarithmic region. It was noted earlier that the instantaneous velocity in this small region could be negative and the mean velocity deduced from the Pitot-tube data in this region can be larger than the actual value. Considering this, it may be concluded that the mean velocities in the present boundary layers are in good agreement with the Perry–Schofield profile provided that the pseudo-shear-stress profile is used to define the scaling parameters.

As noted earlier, the surface curvature near the trailing edge is large, especially on the lower surface. Bradshaw (1969) has shown that even mild curvature $(\delta/R_w \approx 0.003)$ can significantly affect the structure and the development of turbulent boundary layers. The values of δ/R_w in the present boundary layers on Model B extend to ± 0.06. These values are almost as large as those of So & Mellor (1973, 1975) who found that, on the convex surface of their curved channel, the turbulence almost died out and three-dimensionality and longitudinal vortices developed on the concave surface. In the present lower-surface boundary layer, several spanwise traverses of
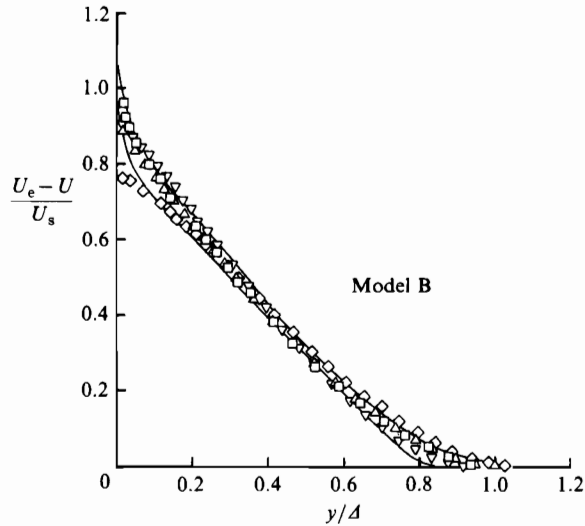
FIGURE 11. Mean-velocity profiles normalized by Perry–Schofield (1973) parameters with normal-stress correction of Simpson *et al.* (1981): □, $X/C = 0.949$; △, 0.97; ▽, 0.99; ◇, 1.0; solid lines are the limits of scatter in data used by Perry & Schofield.

the Preston tube were performed but no evidence of three-dimensionality was found. There are several reasons for these suppressed curvature effects. First, the curvature is not present over long distances. Secondly, the flow direction near the trailing edge is not controlled by the surface direction and, as shown in figure 4, the streamline curvatures are less over most of the boundary layer. This incidentally implies a complicated wall layer with changing flow direction. Furthermore, the pressure gradients are such that they counterbalance the curvature effects. On the upper surface, the adverse pressure gradient tends to enhance turbulence while the convex curvature there tends to suppress it. The opposite phenomenon occurs on the lower surface where the large pressure-gradient parameter implies a tendency to relaminarization but concavity of the surface indicates a very high instability. The present measurements represent an example of a practical flow and are not meant to derive systematic cause-and-effect relations. They simply indicate an urgent need for more studies of such combined effects.

In order to view the above effects in terms of a practical quantity, mixing-length (defined by $l = (-\overline{uv})^{\frac{1}{2}}/(\partial U/\partial y)$) distributions are shown in figures 12(*a*) and (*b*). Those for the boundary layers of the conventional airfoil, Model A, seem to be consistent with those of mild-pressure-gradient flows. With Model B, however, large reductions in the upper-surface boundary layer and large increases in the lower-surface boundary layer can be seen in the trailing-edge region.

Simpson *et al.* (1981*a*) suggested that the reduction in mixing length in a boundary layer approaching separation, such as the present boundary layer on the upper surface of Model B, is due to the importance of the turbulent energy production associated with the normal stresses. They gave an empirical relation:

$$\frac{l}{\delta} = F^{-1.25} \frac{l}{\delta}\bigg|_{F=1}, \tag{7}$$

where

$$F = 1 - \frac{(\overline{u^2} - \overline{v^2}) \, \partial U/\partial x}{-\overline{uv} \, \partial U/\partial y}, \tag{8}$$
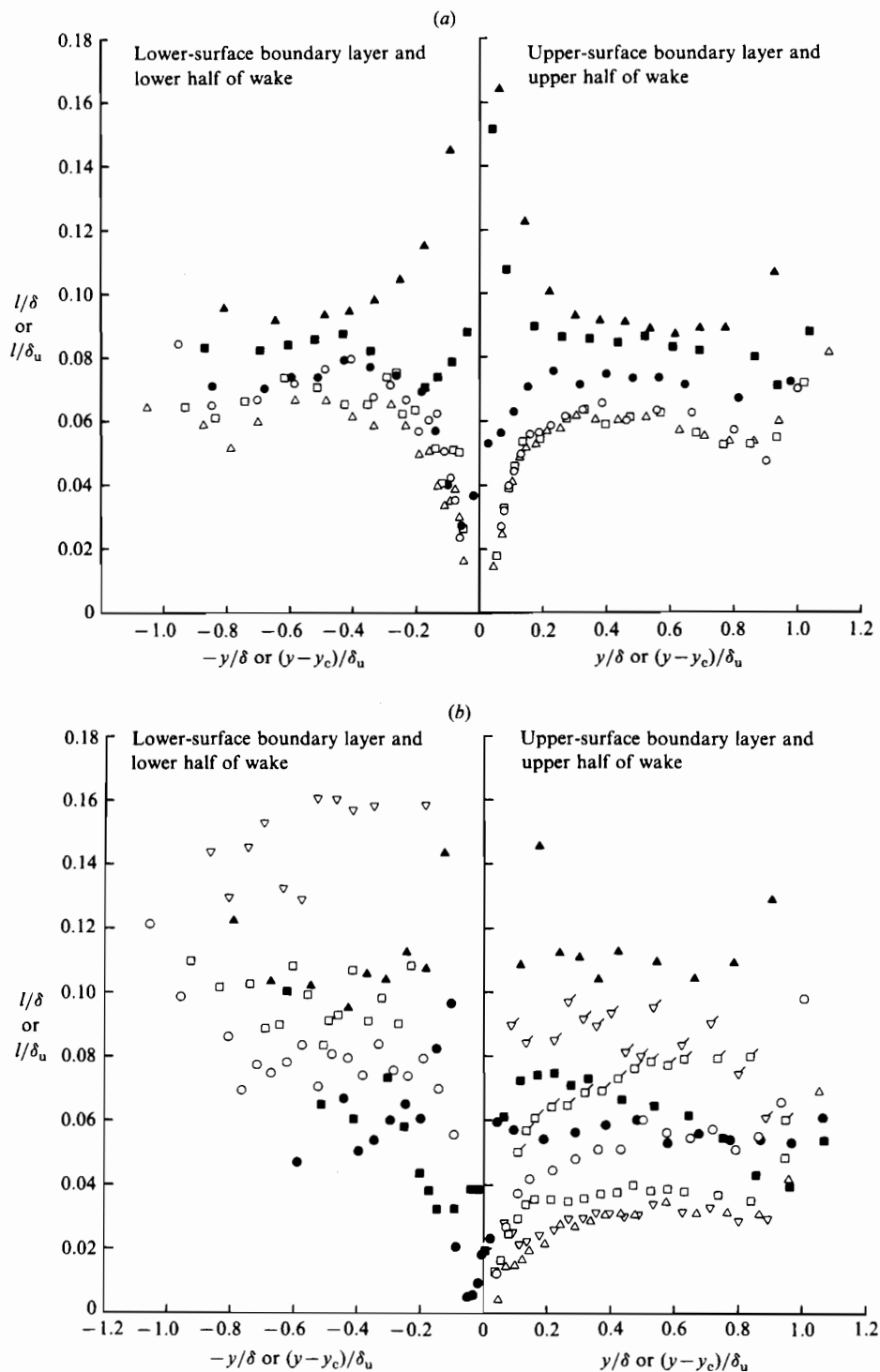
FIGURE 12. Mixing-length distributions, (a) Model A, (b) Model B: $\bigcirc$, $X/C = 0.893$; $\square$, 0.97; $\triangle$, 0.99; $\triangledown$, 1.0; $\bullet$, 1.01; $\blacksquare$, 1.05; $\blacktriangle$, 1.20; flags indicate the mixing length $l/\delta|_{F-1}$ calculated from (7).
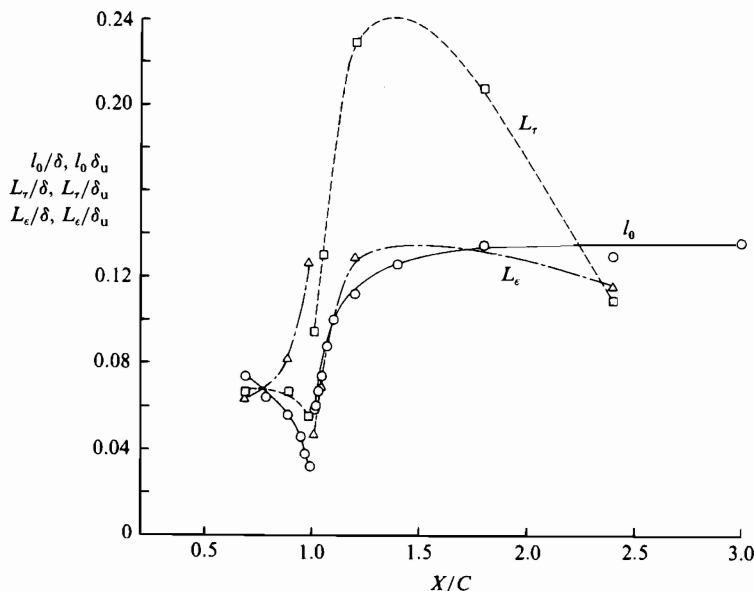
FIGURE 13. Streamwise variation of dissipation lengths $L_\tau \equiv (-\overline{uv})^{\frac{3}{2}}/\epsilon$, and $L_\epsilon \equiv (\overline{q^2})^{\frac{3}{2}}/\epsilon$ and mixing length l_0 in the outer part of the upper-surface boundary layer and upper half of the wake of Model B: ◯, l_0/δ; □, L_τ/δ; △, L_ϵ/δ.

and $l/\delta|_{F-1}$ is the mixing length in a boundary later with $F = 1$, i.e. negligible energy production due to normal stresses. In order to examine the above correlation, $l/\delta|_{F-1}$ was calculated from the measured l/δ and F using (7), for the upper-surface boundary layer of Model B and indicated by flagged symbols in figure 12 (b). The values of $l/\delta|_{F-1}$ in the outer layer are seen to take the values of 0.08, the normally accepted value for $l/\delta|_{F-1}$. Equation (7) was established for adverse pressure gradients and the increase in l/δ in the lower-surface boundary layer cannot be correlated with this equation.

In addition to the Prandtl mixing length, the lengthscale of Townsend (1975) $L_\epsilon (\equiv (\overline{q^2})^{\frac{3}{2}}/\epsilon)$, where $\overline{q^2}$ is twice the turbulent kinetic energy per unit mass and ϵ is the rate of dissipation of turbulent kinetic energy, was calculated for the upper-surface boundary layer of Model B using ϵ determined from the difference in the balance of turbulent kinetic energy. The results are shown in figure 13, which also shows the streamwise variation of the dissipation length $L_\tau \equiv (-\overline{uv})^{\frac{3}{2}}/\epsilon$ used by Bradshaw, Ferris & Atwell (1967) and the variation of l_0, the value of l at the position of y where l takes a near-level value in the outer layer excluding the edges. The behaviour of L_τ in the upper-surface boundary layer is seen to be close to that of l_0. In the wake, on the other hand, L_ϵ and l_0 are seen to behave similarly. The opposite trend seen in the variations of L_ϵ and L_τ in the boundary layer implies that the parameter $a_1 \equiv -\overline{uv}/\overline{q^2}$ changes by a large magnitude in this boundary layer. The distributions of the parameter a_1 are shown in figure 14. In the boundary layers of the conventional airfoil, Model A, a_1 is nearly 0.15 while in the upper-surface boundary layer of Model B it decreases substantially near the trailing edge. The shear stress and a_1 are sensitive to small changes in this coordinate direction. Hence parts of the changes in these quantities may be due to a simple rotation of the chosen coordinates rather than the changes in the turbulence structure. In order to see if it is the case a_1 has been recalculated in coordinates tied to the mean-flow characteristics instead of the surface direction. Figure 14 shows the parameter a_1 defined in the coordinates
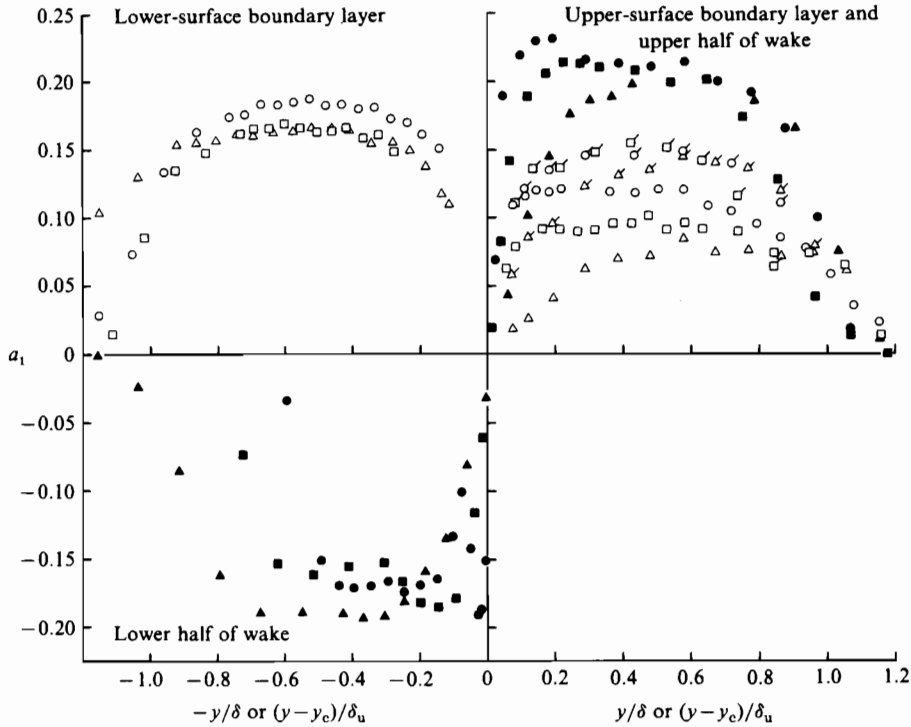
FIGURE 14. Distribution of parameter $a_1 \equiv -\overline{uv}/\overline{q^2}$ in the boundary layers and wake of Model B:
○, $X/C = 0.693$; □, 0.893; △, 0.97; ▽, 0.99; ●, 1.01; ■, 1.05; ▲, 1.20; flags indicate a_1 defined
by the shear stress in the coordinates rotated by the angle that the principal axis of
mean-rate-of-strain tensor deviates from $45°$ to the surface.

that rotate in the same way as the principal axis of the mean-strain tensor. They are
indicated by the flagged symbols, and are seen to take values close to 0.15 over much
of the outer layer. It indicates that the reduction in a_1, seen earlier, was mainly due
to the (artificial) coordinates based on the local surface.

In the near wake there are three layers which can be described as the continuation
of the two upstream boundary layers and a newly developing mixing zone between
them. These three layers have different velocity and lengthscales which influence
each other and change with location. The effective velocity $u_{\tau\,\mathrm{eff}}$ shown in figure 5,
for example, appears to be influenced by the $u_{\tau\,\mathrm{eff}}$ associated with the flow on the
other side. The characteristics of the inner wake were explored in detail by
Andreopoulos & Bradshaw (1980) in simple cases without pressure gradients. In the
present wakes where asymmetry is created by the pressure gradient, the behaviour
is quite different. In the strong asymmetric near-wake of Model B, the turbulence
generated in the inner mixing zone spreads and dominates the lower half of the wake
downstream (see figure 7b). The mixing length takes a minimum value in this mixing
zone. Figure 15 shows the streamwise variation of this minimum value. It increases
linearly as in a plane mixing layer between two streams. As this inner mixing region
develops, the asymmetry in both mean-velocity and Reynolds-stress profiles quickly
disappears. It is interesting to note that the thicker side of the wake actually becomes
thinner. This rapid tendency towards symmetry occurs over distances about 100
times the viscous-sublayer thickness at the trailing edge for both cases. Figure 15 also
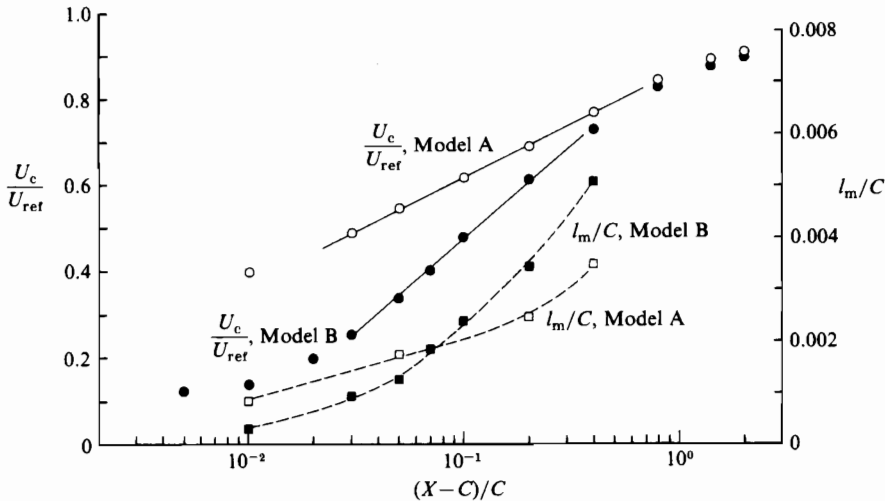
FIGURE 15. Development of the minimum velocity U_c and minimum mixing length l_m in the wakes of two models.

shows that the wake minimum velocity after this rapid-adjustment region increases logarithmically up to about $X/C = 1.8$. It was found for both cases that the self-preservation of the mean velocity and Reynolds stresses start at about $X/C = 1.8$.

8. Conclusions

The mean-velocity, pressure and turbulent-stress fields near the trailing edges of two airfoils in incompressible flow of a chord Reynolds number of 1.2×10^6 have been obtained and analysed to clarify the characteristics of the mean-velocity and turbulent-stress fields.

The results of the survey revealed a number of characteristics of attached flows around conventional and supercritical airfoils. In the former case the boundary layers experience only mild adverse pressure gradients, and the wake development is similar to that behind a flat plate. In the latter case the qualitative pattern of the pressure field near the trailing edge, is distorted, which, in turn, induces a strong asymmetry of the boundary layers and the wake. The region of significant normal pressure gradient was found to exist upstream and downstream of the trailing edge to approximately twice the width of the wake at the trailing edge. In this region the flow directions are forced to change partly by the surface and partly by the freestream. The streamwise pressure gradient is strong and streamline curvatures are large. The flow appears to be changing rapidly but the mean-velocity profiles in the decelerated boundary layer on the upper surface were found to collapse onto the Perry–Schofield (1973) profile if the modification suggested by Simpson *et al.* (1977) is made. As the trailing edge is approached, the Reynolds shear stress, the shear correlation coefficient, the mixing length and the dissipation length L_τ were all found to be small compared with other boundary layers in mild pressure gradients. Opposite trends were seen in the lower-surface boundary layer. The Reynolds-stress components strongly depend on the way the coordinates are chosen. However, at least the structure parameter representing the ratio of shear stress to turbulent kinetic energy

preserves some similarity in the coordinate system tied to the directions of the principal axes of mean-rate-of-strain tensor.

The characteristics of the wakes of the two models were also found to be different. The wake of Model A is not widely different from wakes of flat plates and symmetric airfoils. The wake of the supercritical-airfoil model presents very strong asymmetric features.

In the region near the wake centreline, and immediately downstream of the trailing edge, the interaction of two merging boundary layers creates an intense mixing zone where the flow changes rapidly with increased turbulence intensity and shear stress. The rapid changes slow down quickly over distances of around 100 times the viscous-sublayer thickness at the trailing edge. In both wakes, there is an intermediate region where the rapid smoothing near the centreline has died out but the overall asymmetry still exists and the slower changes towards the self-preservation take place up to about 80 % of chord downstream of the trailing edge. The lengthscale of turbulence depends more on the distance from the trailing edge than on the lengthscale of the local mean quantities. The minimum velocity U_c grows nearly logarithmically with larger slope for higher asymmetry.

REFERENCES

ADAIR, D., THOMPSON, B. E. & WHITELAW, J. H. 1983 *Numerical and Physical Aspects of Aerodynamic Flows II* (ed. T. Cebeci), pp. 97–112. Springer.

ANDREOPOULOS, J. & BRADSHAW, P. 1980 *J. Fluid Mech.* **100**, 639.

BAKER, A. J., YU, J. C., ORZECHOWSKI, J. A. & GATSKI, T. B. 1982 *AIAA J.* **20**, 51.

BRADSHAW, P. 1969 *J. Fluid Mech.* **36**, 177.

BRADSHAW, P. 1971 *An Introduction to Turbulence and Its Measurement.* Pergamon.

BRADSHAW, P. 1975 *ASME* I: *J. Fluids Engng* **97**, 146.

BRADSHAW, P., FERRISS, D. H. & ATWELL, N. P. 1967 *J. Fluid Mech.* **28**, 593.

BREDERODE, V. DE & BRADSHAW, P. 1978 *ASME* I: *J. Fluids Engng* **100**, 91.

CHEVRAY, R. & KOVASZNAY, L. S. G. 1969 *AIAA J.* **1**, 1641.

CLEARY, J. W., VISWANATH, P. R., HORSTMAN, C. C. & SEEGMILLER, H. C. 1980 *AIAA Paper* 80–1396.

DEIWERT, G. S. 1978 *NASA TM* 78581.

FINNIGAN, J. J. 1983 *J. Fluid Mech.* **130**, 241.

HAH, C. & LAKSHIMINARAYANA, B. 1982 *J. Fluid Mech.* **115**, 251.

JOHNSON, D. A. & SPAID, F. 1983 *J. Aircraft* **20**, 298.

MELNIK, R. E., CHOW, R. & MEAD, H. R. 1977 *AIAA Paper* 77–680.

NAKAYAMA, A. 1983 *Numerical and Physical Aspects of Aerodynamic Flows II* (ed. T. Cebeci), pp. 233–255. Springer.

PATEL, V. C. 1965 *J. Fluid Mech.* **23**, 185.

PATEL, V. C. & SCHEUERER, G. 1982 *AIAA J.* **20**, 900.

PERRY, A. E. & SCHOFIELD, W. H. 1973 *Phys. Fluids* **16**, 2068.

POPE, S. B. & WHITELAW, J. H. 1976 *J. Fluid Mech.* **73**, 9.

POT, P. J. 1979 *Proc. 2nd Conf. on Turbulent Shear Flows, Imperial College, London.*

RAMAPRIAN, B. E., PATEL, V. C. & SASTRY, M. S. 1982 *AIAA J.* **20**, 1228.

SIMPSON, R. L., CHEW, Y.-T. & SHIVAPRASAD, B. G. 1981*a* *J. Fluid Mech.* **113**, 23.

SIMPSON, R. L., CHEW, Y.-T. & SHIVAPRASAD, B. G. 1981*b* *J. Fluid Mech.* **113**, 53.

SIMPSON, R. L., STRICKLAND, J. H. & BARR, P. W. 1977 *J. Fluid Mech.* **79**, 553.

SO, R. M. C. & MELLOR, G. L. 1973 *J. Fluid Mech.* **60**, 43.

SO, R. M. C. & MELLOR, G. L. 1975 *Aero. Quart.* **16**, 25.

SPAID, F. W. & HAKKINEN, R. J. 1977 *J. Appl. Math. Phys.* **28**, 941.

TOWNSEND, A. A. 1975 *The Structure of Turbulent Shear Flow*, 2nd edn. Cambridge University Press.

VISWANATH, P. R. & BROWN, J. L. 1983 *AIAA J.* **21**, 801.

VISWANATH, P. R., CLEARLY, J. W., SEEGMILLER, H. C. & HORSTMAN, C. C. 1979 *AIAA Paper* 79–1503.

YU, J. C. 1981 *NASA TP*-1845.

WADCOCK, A. J. 1980 *NASA CR* 3283.

WU, J. C. & GULCAT, U. 1981 *AIAA J.* **19**, 20.